\$50 CH ELSEVIER

Contents lists available at ScienceDirect

Ocean Engineering

journal homepage: www.elsevier.com/locate/oceaneng



Control co-design optimization of nonlinear wave energy converters[☆]

Habeebullah Abdulkadir*, Ossama Abdelkhalik

Department of Aerospace Engineering, Iowa State University, Ames, IA 50010, USA

ARTICLE INFO

Keywords: Wave energy converter Optimal control Control co-design Nonlinear WEC Froude–Krylov forces

ABSTRACT

This paper presents a study in which both the control and the shape of a Wave Energy Converter (WEC) are optimized simultaneously. A heaving point absorber WEC is assumed. To optimize the shape of the WEC's buoy, nonlinear hydrodynamics need to be evaluated. One main contribution of this paper is the integration of nonlinear hydrodynamics and nonlinear control during the optimization of the WEC's buoy shape. This approach is referred to as Control Co-Design (CCD). In this work, we present a control co-designed nonlinear heaving point absorber WEC that leverages the nonlinear dynamic, static Froude–Krylov (FK) forces to maximize power extraction. The nonlinear FK forces are approximated using a variation of the algebraic solution; the hydrodynamic forces of the body are computed using an analytic formulation leveraging the methods of eigenfunction expansion and separation of variables. The nonlinear geometry of the buoy is modeled as a series of inclined panels; the inclination angles are optimized to arrive at the optimal shape. The performance of the optimized shape is compared to that of a nonlinear spherical WEC. It is found that an average of 20% improvement is achieved by the optimized geometry over the spherical device.

1. Introduction

Point absorber WECs are generally characterized by dimensions smaller than the wavelength of incoming waves. These devices extract energy from the relative motion between the floating buoy and their relatively fixed submerged base. Maximum energy extraction is achieved when the floater resonates with the exciting wave. Since the interaction between these device structures and the wave determines the quantity of power generation, geometric optimization to improve the hydrodynamic performance of wave–structure interaction (WSI) becomes important for these devices to improve their efficiency. Detailed review on geometric optimization of point absorbers is presented in Guo and Ringwood (2021a), and Garcia-Teruel and Forehand (2021).

To enable WEC technologies to reach commercial maturity within the renewable energy sector, the Levelized Cost of Energy (LCoE) must become competitive with other renewable energy alternatives. Optimizing the structural design, the geometry (shape and size), and the control were some of the identified ways for cost reduction in developing WECs by Ochs and Bull (2013). WEC optimization and control have primarily relied on linear models, mostly due to the associated computational cost. However, to obtain more practical results, some critical nonlinear

factors should be considered (Korde and Ringwood, 2016). Nonlinearities in the WEC dynamic model can be from different sources; the source of nonlinearity considered in this work is the hydrodynamic nonlinearity resulting from geometries with non-constant water surface area.

WEC design is traditionally sequential; control engineers generally design and tune the controllers after the wave energy converter has been completely designed. The works in Zou et al. (2023), Bacelli et al. (2015), Giorgi and Ringwood (2018), Na et al. (2018), Wilson et al. (2018, 2020), Abdelkhalik and Darani (2018), Demonte Gonzalez et al. (2021), Richter et al. (2012) have developed several innovative formulations of controller for WECs subject to different nonlinearities. However, there is often a mismatch in the system's performance due to different controllers used during the initial design optimization and the energy-maximizing control implemented during the final deployment of the device; it has been observed that the several stages of WEC design and control development are inherently and non-linearly coupled (Davidson et al., 2019), and a co-design approach is needed (Guo and Ringwood, 2021b). A control co-design approach that simultaneously optimizes the system and the final control design has been shown to yield superior results in various fields of engineering (O'Sullivan and

E-mail address: habeeb19@iastate.edu (H. Abdulkadir).

URL: https://www.aere.iastate.edu/ossama/ (O. Abdelkhalik).

This paper is based upon work supported by National Science Foundation, Grant Number 2048413. The research reported in this paper is partially supported by the HPC@ISU equipment at Iowa State University, some of which has been purchased through funding provided by National Science Foundation under MRI grant number 1726447.

^{*} Corresponding author.

Lightbody, 2017; Garcia-Sanz, 2019; Jin et al., 2019; Coe et al., 2020; Pao et al., 2021; Giannini et al., 2022).

The main focus of this work is the concurrent design optimization of a heaving WEC geometry and energy-maximizing control that leverages hydrodynamic nonlinear forces to improve the overall power harvested from the waves. The hydrodynamic nonlinearities considered result from the geometry having a varying cross-sectional area along the water surface, as in the case of a spherical device. In the case of a heaving cylindrical geometric shape, the hydrostatic and dynamic forces are calculated over a constant wetted area as the geometry at the water surface is constant; however, with varying geometry at the water surface, the pressure needs to be integrated over the submerged surface instantaneously. The resulting hydrodynamic forces are called the Froude-Krylov (FK) forces. Generally, to compute these forces at every instant using the boundary element method or CFD would require remeshing the submerged geometry at every step, which would be computationally expensive. So, for ease of computing the nonlinear FK forces, a closed-form algebraic approximation of nonlinear Froude-Krylov (NLFK) force developed in Giorgi and Ringwood (2017), Giorgi et al. (2021) was adopted. A more computationally expensive remehsing method was used to derive the nonlinear FK forces (the static and dynamic pressure forces) acting on a buoy within 2% error to the analytical approach.

An analytic approach that is based on the principle of variable separation and eigenfunction expansion was developed to compute the hydrodynamic coefficients of the changing geometry during the optimization. The computational expense incurred from computing new hydrodynamic coefficients of the changing geometry is a well-known bottleneck for geometric optimization (especially irregular waves). The computational cost from using numerical boundary element method (BEM) routines such as Aqwa (ANSYS, 2013), NEMOH (Babarit and Delhommeau, 2015), and WAMIT (WAMIT User Manual, 2013) is significant and grows exponentially as the number of devices increases. The analytic approach can accurately compute the hydrodynamic coefficients assuming potential flow. Since nonlinear exciting forces (NLFK) are considered on the geometries, the analytical method would only be used to solve the radiation problem (the added mass and damping) contributions from linear wave radiation, while the nonlinear diffraction and hydrostatics will be solved using the algebraic method discussed earlier.

The paper is organized as follows. In Section 2, the linear and non-linear dynamic model of a simplified WEC is established. In Section 3, the formulation of the analytical method to compute the hydrodynamic coefficients is presented. Section 4 shows the control co-design problem formulation. Simulation and results are presented in Section 5, and finally, conclusions are presented in Section 6.

2. WEC dynamic modeling

In this section, the formulation of a linear model for a heaving WEC is presented, and then the formulation for the algebraic approximation for the nonlinear FK forces is introduced. Based on the nonlinear FK formulation, the nonlinear dynamic model is presented.

2.1. Linear model

Applying Newtow's second law of motion to modeling a single degree of freedom WEC yields the equation:

$$m\ddot{z} = f_e + f_r + f_{visc} + f_h + u \tag{1}$$

where m is the mass of the buoy,

$$f_e = \int_{-\infty}^{\infty} h_f(\tau) \eta(t - \tau, z) d\tau$$

is the excitation force; η is the wave elevation, and h_f is the excitation impulse response function. The viscous loss is modeled as additional

linear damping as $f_{visc} = B_{visc}\dot{z}$. The hydrostatic restoring force, $f_h = Kz$, u is the linear control force.

$$f_r = -m_{\infty} \ddot{z}(t) - \int_{-\infty}^t h_r(\tau) \dot{z}(t-\tau) d\tau$$

is the radiation force, with m_{∞} as the added mass at infinite frequency, and h_r is the radiation impulse response function. The radiation term can be approximated in state-space as (Jefferys, 1984).

$$\dot{z}_r = A_r \vec{z}_r + B_r \dot{z} \tag{2}$$

$$f_r = C_r \vec{z}_r \tag{3}$$

where $\vec{z}_r \in \mathbb{R}^{n_r \times 1}$ is the radiation state vectors, $A_r \in \mathbb{R}^{n_r \times n_r}$, $B_r \in \mathbb{R}^{n_r \times 1}$, and $C_r \in \mathbb{R}^{1 \times n_r}$ are the radiation matrices and n_r is the order of the radiation system. To write the radiation states augmented equation of motion in a compact state space form, we define the state vectors as follows:

$$\vec{z} = [z_1, z_2, \vec{z}_r]^T$$

where z_1 is the displacement, z_2 is the velocity, and \vec{z}_r is the vector of radiation states. The state space form of the equations of motion can now be written as:

$$\begin{cases} \dot{z}_1 \\ \dot{z}_2 \\ \dot{\bar{z}}_r \end{cases} = A \begin{cases} z_1 \\ z_2 \\ \ddot{z}_r \end{cases} + Bu + Bf_e$$
 (4)

where

$$B = \begin{bmatrix} 0 \\ -[m+m_{\infty}]^{-1} \\ 0 \end{bmatrix}$$
 (5)

$$A = \begin{bmatrix} 0 & 1 & \mathbf{0} \\ -[m+m_{\infty}]^{-1}K_h & -[m+m_{\infty}]^{-1}B_{visc} & -[m+m_{\infty}]^{-1}C_r \\ 0 & B_r & A_r \end{bmatrix}$$
(6)

2.2. Nonlinear Froude-Krylov forces and nonlinear model

In modeling point absorber wave energy converters, many works use linear hydrodynamic approximations, even for nonlinear geometries like a spherical floater, due to the complexity and computation cost associated with nonlinear hydrodynamic modeling. However, the inaccuracy in the linear model grows when linear assumptions like small amplitude motion and constant area at the water surface fail. For axis-symmetric point absorbers, the Froude-Krylov (FK) force was found to be the most relevant nonlinear component of the hydrodynamic force. In a linear model, the excitation force is composed of the hydrodynamic Froude-Krylov force and the diffraction force computed over a constant mean wetted surface of the floater. However, for the nonlinear model, the hydrodynamic Froude-Krylov force is computed at every time instance while the diffraction component is assumed to be 0; this is due to the assumption that the characteristic length of heaving point absorber WECs is much smaller than the wavelength which means the device does not impact the wave field.

These nonlinear forces lead to quite significant changes in the trajectory and magnitude of the motion of a linear and nonlinear device. The physics captured in nonlinear models results in more accurate force modeling, which leads to a more realistic response trajectory. For an arbitrary geometry like Fig. 1, the mean wetted surface changes instantaneously.

Rather than having to remesh and recalculate the FK forces on the instantaneously changing geometry which could result in high computation cost, Giorgi and Ringwood (2017) developed algebraic calculation of the nonlinear FK forces applicable to axisymmetric heaving point absorbers. The total Froude–Krylov (FK) force is the hydrostatic force FK_{st} and the dynamic force FK_{dy} . The FK forces are computed by

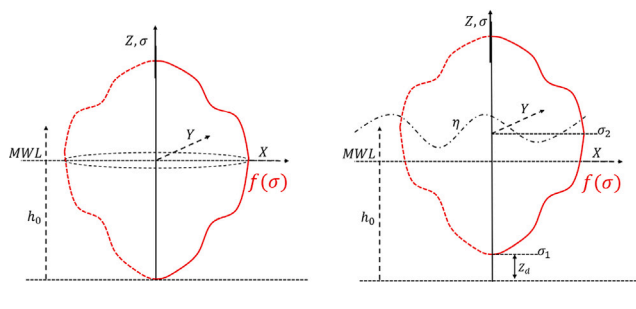


Fig. 1. Axisymmetric heaving device with generic profile.

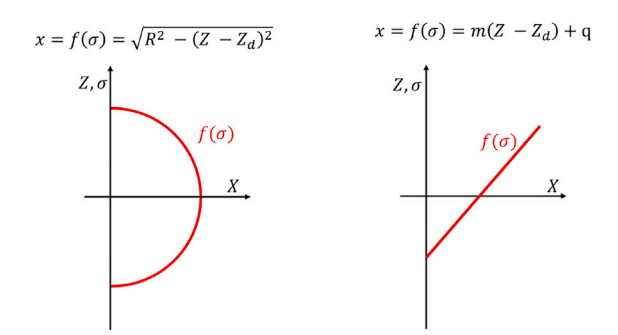


Fig. 2. Shape profiles

integrating the wave pressure from the incident wave over the wetted

$$F_{FK} = F_g - \int_0^{2\pi} \int_{\sigma_1}^{\sigma_2} P(t) \mathbf{n} dS \tag{7}$$

P(t) is the instantaneous pressure, on the infinitesimal element ndS. The total pressure for deep water waves using Airy's wave theory is defined as:

$$P(t) = \rho g e^{\chi \sigma} \eta(t) cos(\omega t) - \rho g \sigma(t)$$
 (8)

where ρ is the water density, g is the gravitational acceleration, $\eta(t)$ is the free surface elevation, χ is the wave number, σ is the heave direction (positive upwards), and ω is the wave frequency. The difference between the gravity force F_g and the static FK force on the buoy is the nonlinear hydrostatic force. The magnitude of the heaving Froude–Krylov forces becomes:

$$F_{FK} = \int_0^{2\pi} \int_{\sigma_1}^{\sigma_2} P(t) f'(\sigma) f(\sigma) d\sigma d\theta \tag{9}$$

$$F_{FK} = \int_{0}^{2\pi} \int_{\sigma_{1}}^{\sigma_{2}} (\rho g e^{\gamma \sigma} \eta(t) cos(\omega t) - \rho g \sigma(t)) f'(\sigma) f(\sigma) d\sigma d\theta$$
 (10)

At the equilibrium position, h_0 is the draft of the buoy, $Z_d(t)$ is the instantaneous displacement of the buoy from its equilibrium position. The algebraic FK forces for the spherical and sloped line profiles described in Fig. 2 can be computed using the equations defined in Eq. (10). The limit of integration based on the free surface elevation and the draft of the buoy can be described as:

$$\sigma_1 = -h_0 + Z_d(t) - \eta(t), \ \sigma_2 = 0 \tag{11}$$

For example, the nonlinear hydrostatic and hydrodynamic forces of a spherical buoy can be computed as:

$$F_{FK_{static}} = F_g + 2\pi\rho g \left[\frac{(-R + Z_d - \eta(t))^3}{3} - \frac{(-R + Z_d - \eta(t))^2}{2} (Z_d + \eta(t)) \right]$$
(12)

$$F_{FK_{dynamic}} = -\frac{2\pi\rho g\eta(t)}{\chi}cos(\omega t)\left[\left(\sigma - Z_d + \eta(t) - \frac{1}{\chi}\right)e^{\chi\sigma}\right]_{\sigma_t}^{\sigma_2}$$
(13)

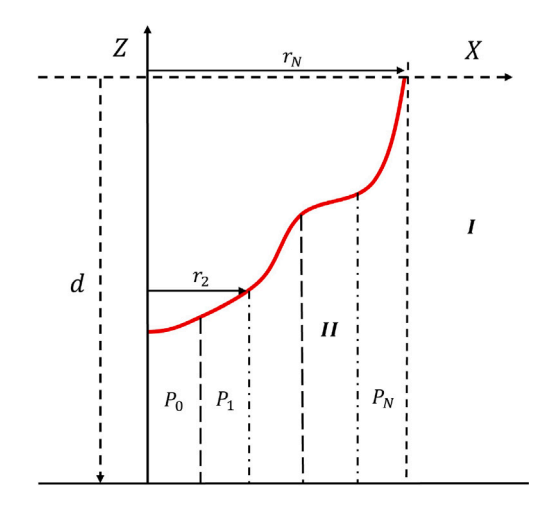


Fig. 3. Fluid domain discretization.

Similarly, the algebraic form of the static and dynamic FK forces can be computed for sloped lines or other shapes that can be represented with algebraic equations. This method of computing FK forces was validated by Giorgi and Ringwood (2017) against a more computationally expensive remeshing method and was found to only have about a 2% error. The overall nonlinear dynamic equation can then be written as:

radiation force
$$f_r$$

$$m\ddot{z}(t) = -\mu \ddot{z}(t) - \int_{-\infty}^{t} h_r(\tau) \dot{z}(t-\tau) d\tau + u$$
NLFK forces
$$-f_{visc} + F_{FK_{dyn} + F_{FK_{st}}}$$
(14)

Following the formulation proposed in Song et al. (2020), a simple nonlinear control is formulated as:

$$u = -\alpha B_{max}(\omega)\dot{z} - \beta B_{max}(\omega)\dot{z}^3 \tag{15}$$

where α and β are control coefficients to be optimized, $B_{max}(\omega)$ is the maximum hydrodynamic damping coefficient on the device and \dot{z} is the heave velocity of the device. The linear radiation problem must still be solved to compute the floating device's added mass and damping coefficients. This radiation problem can also be solved analytically using the variable separation method and eigenfunction expansion described in the following subsection.

3. Analytic method of solving the hydrodynamic radiation prob-

The theory for the radiation problem of a floating arbitrary shape is described in this section. This method is based on discretizing the fluid domain around the device into small panels, for which the velocity potential for each of these panels is approximated with a Fourier series. This method is an improvement on the method used for solving the hydrodynamic problem of floating cylinders as in Yilmaz (1998), McNatt et al. (2015), Child and Venugopal (2010).

Consider a buoyant axis-symmetric object undergoing harmonic oscillations in water with a depth d, as depicted in Fig. 3. The maximum submerged depth of the body in consideration is h_0 . The horizontal mean water surface is defined as the Oxy plane, and polar coordinates (r,θ) in the horizontal plane are established with the Oz-axis oriented upwards. Employing linear wave theory, characterized by incompressible, inviscid, and irrotational flow assumptions, the velocity potential throughout the fluid is represented using a complex form:

$$\Phi(r,\theta,z,t) = Re\{\phi(r,\theta,z)\}e^{-i\omega t}$$
(16)

Here, $Re\{\}$ represents the real part of the complex expression, and t signifies the time dependence. For it to qualify as a legitimate solution, the spatial velocity potential $\phi(r, \theta, z)$ must adhere to the Laplace equation and the linearized boundary conditions:

- The Laplace equation

$$\nabla^2 \phi = 0 \tag{17}$$

- Free surface conditions

$$\omega^2 \phi - g \frac{\partial \phi}{\partial z} \Big|_{z=0} = 0 \tag{18}$$

- Sea bed condition

$$\left. \frac{\partial \phi}{\partial z} \right|_{z=-d} = 0 \tag{19}$$

- Impermeable condition on the body surface

$$\frac{\partial \phi}{\partial r} = 0, \ (r = r_N, -h \le z \le 0) \tag{20}$$

$$\frac{\partial \phi}{\partial z} = 0, \ (0 \le r \le r_N, z = -h) \tag{21}$$

- Body surface condition

$$\nabla \phi . \vec{n} = \vec{U} . \vec{n} \tag{22}$$

where \vec{U} is the velocity of the body, and \vec{n} is the unit normal vector on the body.

- The Sommerfeld radiation condition:

$$\lim_{x \to \infty} \sqrt{r} \left(\frac{\partial \phi}{\partial r} - i k_n \phi \right) = 0 \tag{23}$$

where k_n is the wave number solved from the dispersion relation:

$$\omega^2 = gktanh(kd) \tag{24}$$

the positive real solution, identified as k_0 , represents the wavenumber of the progressive mode. The negative imaginary solutions, denoted as k_n for n=1,2,..., correspond to the wavenumbers of the evanescent modes (Chamberlain and Porter, 1999). The comprehensive velocity potential for the entire fluid domain can be decomposed as follows:

$$\phi(r,\theta,z) = \phi_0(r,\theta,z) + \phi_7(r,\theta,z) + \sum_{q=1}^{6} \phi_q(r,\theta,z)$$
 (25)

where ϕ_0 is the incident wave potential, ϕ_7 is the diffracted potential, ϕ_q and is the radiated potential due to the motion of the body in the direction, q=1,3,5 corresponding to surge, heave, and pitch mode of motion, respectively. However, due to our current problem formulation, we will only be solving the radiation problem, as the NLFK force will be computed using an algebraic method. To achieve this, the fluid region will be separated into the interior (II) and exterior regions (I), the fluid region away from the body maximum radius and the region below the shape, respectively as in Fig. 3. The interior region further decomposed into vertical panels. Apart from the inability of this method to account for nonlinear diffraction, other limitation includes difficulty in dealing with complex geometries, limitation in capturing strong coupling effects between fluid and body, and increase in computation cost as the body becomes more complex or deployment for arrays.

3.1. Radiation problem

The radiation scenario pertains to a situation in which the body is positioned in undisturbed water, devoid of any incoming waves, and is subsequently compelled to oscillate. The overall radiation potential:

$$\phi_{q}(r,\theta,z) = \sum_{m=-\infty}^{\infty} i\omega H \varphi_{q,m}(r,z) cos(m\theta)$$
 (26)

where H represents the complex amplitude associated with the motion mode. In the heaving mode (q = 3), only terms with m = 0 contribute. Therefore, we are seeking solutions that can be formulated as:

$$\varphi_{3,m}(r,z) = \varphi_{3,h} + \varphi_{3,p} \tag{27}$$

where $\varphi_{3,p}$ denotes a particular solution of the velocity potential in the heave mode, and $\varphi_{3,h}$ constitutes the homogeneous component of the solution for the boundary value problem. The potential function for each respective region can be decomposed as follows.

3.1.1. Interior region

The interior region's homogeneous potential can be written as:

$$\varphi_{3,h}^{I_0} = \frac{C_{R0}^0}{2} \left(\frac{r}{r_0}\right)^m + \sum_{n=1}^{\infty} C_{Rn}^0 \frac{I_m(\frac{n\pi r}{(d-h_0)})}{I_m(\frac{n\pi r_0}{(d-h_0)})} cos(\frac{n\pi z}{(d-h_0)})$$
(28)

when the innermost panel, P_0 is considered and,

$$\varphi_{3,h}^{I_p} = \sum_{n=0}^{\infty} \left[C_{Rn}^p S_n + \tilde{C}_{Rn}^p \tilde{S}_n \right] \cos(\frac{n\pi z_p}{(d-h_p)}) \quad \forall \quad p \in [1 \ N]$$
 (29)

for $p \in [1 \ N-1]$,

$$S_{0} = \frac{\left(\frac{r}{R_{p}}\right)^{m} - \left(\frac{R_{p}}{r}\right)^{m}}{\left(\frac{R_{p+1}}{R_{p}}\right)^{m} - \left(\frac{R_{p}}{R_{p+1}}\right)^{m}}, \quad \tilde{S}_{0} = \frac{\left(\frac{R_{p+1}}{r}\right)^{m} - \left(\frac{r}{R_{p+1}}\right)^{m}}{\left(\frac{R_{p+1}}{R_{p}}\right)^{m} - \left(\frac{R_{p}}{R_{p+1}}\right)^{m}}$$
(30)

$$S_{n} = \frac{I_{m}(\frac{n\pi r}{(d-h_{p})})K_{m}(\frac{n\pi R_{p}}{(d-h_{p})}) - I_{m}(\frac{n\pi R_{p}}{(d-h_{p})})K_{m}(\frac{n\pi r}{(d-h_{p})})}{I_{m}(\frac{n\pi R_{p+1}}{(d-h_{p})})K_{m}(\frac{n\pi R_{p}}{(d-h_{p})}) - I_{m}(\frac{n\pi R_{p}}{(d-h_{p})})K_{m}(\frac{n\pi R_{p+1}}{(d-h_{p})})}$$
(31)

$$\tilde{S}_{n} = \frac{I_{m}(\frac{n\pi R_{p+1}}{(d-h_{p})})K_{m}(\frac{n\pi r}{(d-h_{p})}) - I_{m}(\frac{n\pi r}{(d-h_{p})})K_{m}(\frac{n\pi R_{p+1}}{(d-h_{p})})}{I_{m}(\frac{n\pi R_{p+1}}{(d-h_{p})})K_{m}(\frac{n\pi R_{p}}{(d-h_{p})}) - I_{m}(\frac{n\pi R_{p}}{(d-h_{p})})K_{m}(\frac{n\pi R_{p+1}}{(d-h_{p})})}$$
(32)

for p = N

$$S_0 = \frac{ln\left(\frac{r}{R_{p-1}}\right)}{ln\left(\frac{R_p}{R_{p-1}}\right)}, \quad \tilde{S}_0 = \frac{ln\left(\frac{R_p}{r}\right)}{ln\left(\frac{R_p}{R_{p-1}}\right)}$$
(33)

$$S_{n} = \frac{I_{m}(\frac{n\pi R_{p}}{(d-h_{p})})K_{m}(\frac{n\pi R_{p-1}}{(d-h_{p})}) - I_{m}(\frac{n\pi R_{p-1}}{(d-h_{p})})K_{m}(\frac{n\pi r}{(d-h_{p})})}{I_{m}(\frac{n\pi R_{p}}{(d-h_{p})})K_{m}(\frac{n\pi R_{p-1}}{(d-h_{p})}) - I_{m}(\frac{n\pi R_{p-1}}{(d-h_{p})})K_{m}(\frac{n\pi R_{p}}{(d-h_{p})})}$$
(34)

$$\tilde{S}_{n} = \frac{I_{m}(\frac{n\pi R_{p}}{(d-h_{p})})K_{m}(\frac{n\pi r}{(d-h_{p})}) - I_{m}(\frac{n\pi r}{(d-h_{p})})K_{m}(\frac{n\pi R_{p}}{(d-h_{p})})}{I_{m}(\frac{n\pi R_{p}}{(d-h_{p})})K_{m}(\frac{n\pi R_{p-1}}{(d-h_{p})}) - I_{m}(\frac{n\pi R_{p-1}}{(d-h_{p})})K_{m}(\frac{n\pi R_{p}}{(d-h_{p})})}$$
(35)

the particular solution.

$$\varphi_{3,p}^{I_p} = \frac{1}{2(d-h_p)} \left[(z_p + d)^2 - \frac{r_p^2}{2} \right]$$
 (36)

where C_{Rn}^{p} are fourier coefficients to be solved for and I_{m} is the modified Bessel function of the first kind order m.

3.1.2. Exterior region

The exterior radiation's homogeneous solution is given as:

$$\varphi^{E}_{3,h} = D_{R0} \frac{H_m(k_0 r)}{H_m(k_0 a)} Z_0(z) + \sum_{q=1}^{\infty} D_{Rq} \frac{K_m(k_q r)}{K_m(k_q a)} Z_n(z) \tag{37} \label{eq:3h}$$

where D_{Rq} are unknown Fourier coefficients. H_m is Hankel function, and K_m is the modified Bessel function of the second kind, both of order m. $Z_q(z)$ is the depth dependency function. The depth dependency function $Z_q(z)$ is normalized to form an orthonormal set of eigenfunctions in the corresponding domain.

$$\langle Z_n(z), Z_q(z) \rangle = \delta_{nq}$$
 (38)

where δ_{nq} is the Kronecker delta.

H. Abdulkadir and O. Abdelkhalik Ocean Engineering 304 (2024) 117827

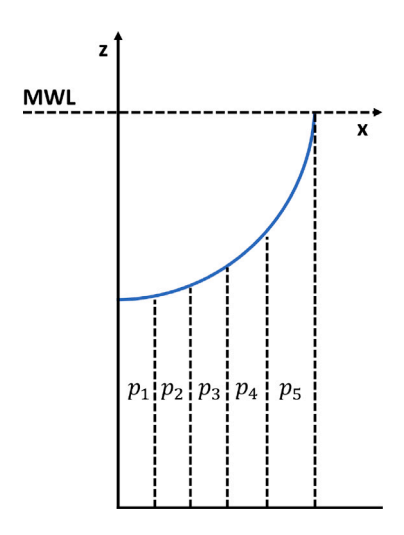


Fig. 4. Arbitrary geometry definition.

3.2. Matching conditions

In addressing the radiation problem, the matching conditions signify the preservation of mass flux, pressure, and normal velocity continuity. The velocity potentials at the interface between the interior and exterior domains are aligned at the imaginary boundary. $r = r_p$.

$$\phi^{I_p} = \phi^{I_{p+1}}, \ (r = r_p, -h_p \le z \le -d)$$
 (39)

$$\frac{\partial \phi^{I_p}}{\partial r} = \frac{\partial \phi^{I_{p+1}}}{\partial r}, \ (r = r_p, -h_p \le z \le -d) \tag{40}$$

$$\phi^{I_{p=N}} = \phi^{E}, \ (r = r_N, -h_N \le z \le -d)$$
 (41)

$$\frac{\partial \phi^I}{\partial r} = \frac{\partial \phi^E}{\partial r}, \ (r = r_N, -h_N \le z \le -d) \tag{42}$$

The unknown Fourier coefficients $C_{Rn}^0, C_{Rn}^p, D_{Rn}$ are solved using the matching conditions. The hydrodynamic coefficients (added mass a_{33} and radiation damping b_{33}) of the device in heave can be calculated and defined by:

$$a_{33} + i \frac{b_{33}}{\omega} = 2\pi \sum_{p=1}^{N} r_p \int_{r_{p-1}}^{r_p} \varphi_3^{I_p}(r, h_p - h) r dr$$
 (43)

More details about this formulation can be found in Zhang et al. (2016), Kokkinowrachos et al. (1986).

3.3. Hydrodynamic coefficients for a sample geometry

To test the present method and its efficiency, the hydrodynamic coefficient of the heaving semi-submerged 5m radius spherical body, as shown in Fig. 4 is computed. For a range of frequencies between $\omega=0.1-6$ rad/s, the hydrodynamic forces are computed. The constant water depth is d=50 m, and the incident wave-heading angle is 0^0 along the x-axis. Since we considered only the radiation problem, the added mass and damping coefficients computed for the device using the analytic formulation and NEMOH BEM software are plotted in Figs. 5 and 6.

4. Control co-design problem formulation

In this section, the control co-design optimization problem is set up. The general goal of this section is to find the optimal geometry and its control, which performs better in a specified wave site. To achieve this, two control co-design problems are formulated; the first is the control

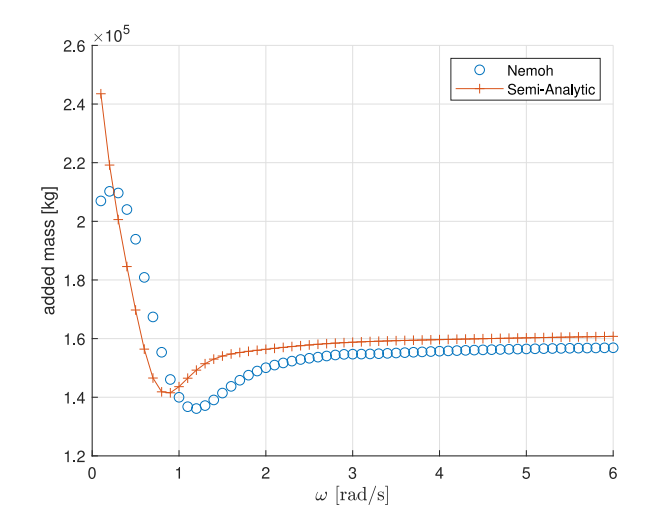


Fig. 5. Added mass coefficients.

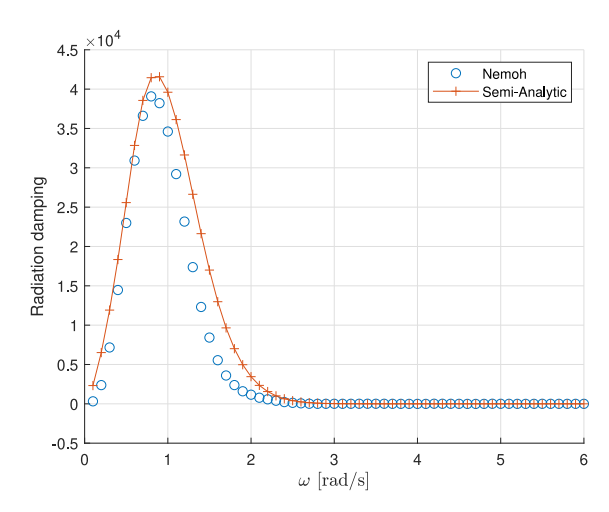


Fig. 6. Damping coefficients.

co-design of a standard spherical WEC where both the dimension and the control are co-optimized for the wave condition of the deployment site. The second control co-design problem is that of arbitrary geometry WEC devices, which intend to find better leverage on the nonlinear forces acting on the devices. The size of the spherical and arbitrary geometry WEC are constrained to be comparable using a set reference volume. The formulations are presented in the following subsections.

4.1. Control co-design for a spherical device

In the current problem, the objective is to determine the optimal radius and control coefficients of the nonlinear control that maximizes the power extraction by the nonlinear spherical device. The instantaneous power captured by the device is computed as the product of the power take-off (PTO) force and velocity of the floater. The optimization objective is the time-averaged power from the device:

$$J = \frac{1}{T} \int_{0}^{t_f} \{-u(t)z_2(t)\} dt$$

$$s.t. \ R \in [R_{min.} \ R_{max.}]$$

$$\alpha_s \in [\alpha_{min.} \ \alpha_{max.}],$$

$$\beta_s \in [\beta_{min.} \ \beta_{max.}],$$
(44)

 $Volume_{sphere} \leq Volume_{Max}$

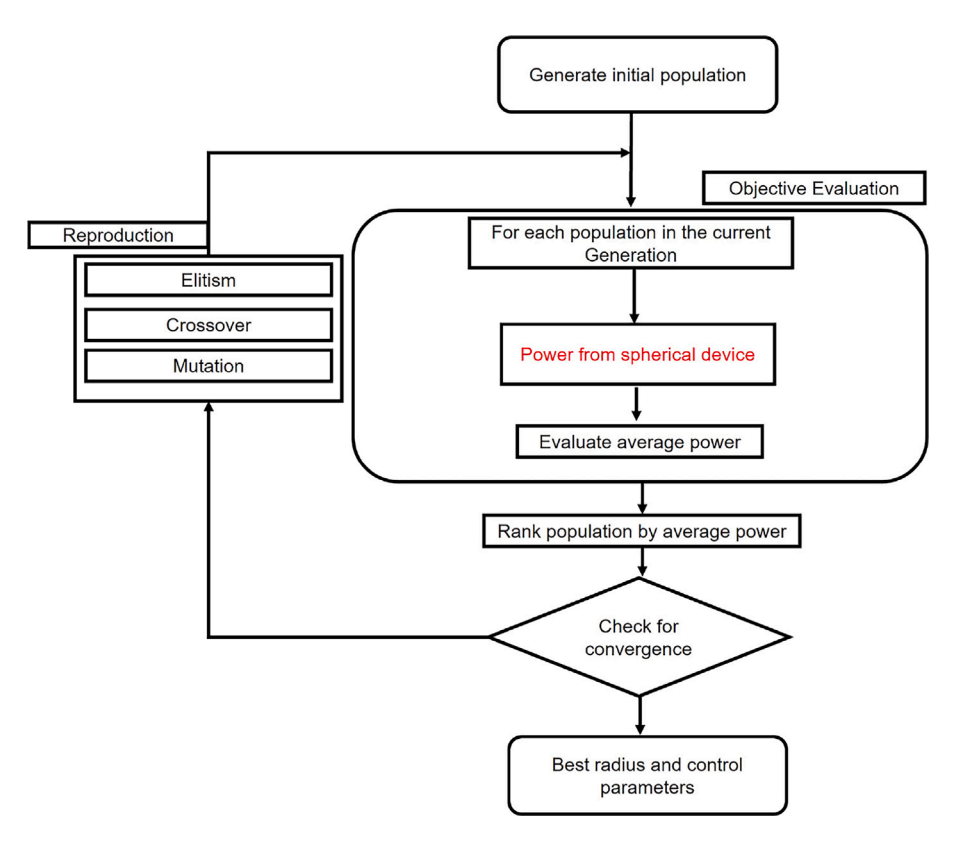


Fig. 7. GA flowchart for control co-design of a nonlinear sphere.

Table 1
Lower and upper bounds of design variables.

Parameter Unit		Lower Bound	Upper Bound	
R	m	2	15	
α_s	-	0.1	3	
β_s	-	0.1	3	

where u is the PTO force, z_2 is the velocity of the device, R is the sphere's radius, α_s and β_s are control coefficients to be optimized, $B_{max}(\omega)$ is the maximum hydrodynamic damping coefficient. The total volume of the sphere is constrained to not exceed a reference volume, which is to be decided by the designer based on economic or technical reasons. The optimization is completed using Genetic algorithm. A flowchart of the optimization setup is presented in Fig. 7. The upper and lower bound of the optimization variables are as presented in Table 1.

4.2. Control co-design for an arbitrary geometry

This section discusses the problem formulation for the control codesign of a more arbitrary geometry that seeks to leverage the nonlinearities to further improve the energy extraction from the waves. The geometry is constructed by connecting several panels end-to-end. The idea of choosing the panel method is the ease of describing individual panels algebraically as a function of their slope and height, which makes it easier to compute the hydrostatic and hydrodynamic FK forces using the method described in Section 2.2. For a geometry symmetrical about the X and Z axes, the parameterization of the nonlinear geometric shape using sloped lines is illustrated in Fig. 8.

The parameters are (1) the draft, (2) a flat horizontal base, and (3–6) which are sloped lines all connected end-to-end. The goal of the optimization is to find the combination of design parameters that maximize the power extraction by the device, subject to constraints.

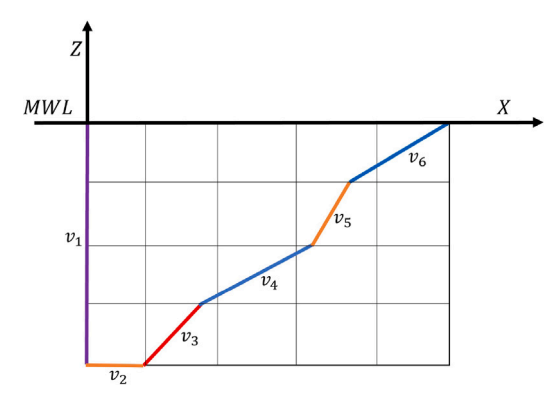


Fig. 8. Arbitrary shape parameterization.

The optimization objective remains the maximization of the P-factor:

$$P = \frac{P_{geometry}}{P_{sphere}}$$

$$s.t. \ v_1 \in [v_{1_{min}} \cdot v_{1_{max.}}],$$

$$v_2 \in [v_{2_{min}} \cdot v_{2_{max.}}]$$

$$v_3 \in [v_{3_{min.}} \cdot v_{3_{max.}}]$$

$$v_4 \in [v_{4_{min.}} \cdot v_{4_{max.}}]$$

$$v_5 \in [v_{5_{min.}} \cdot v_{5_{max.}}]$$

$$v_6 \in [v_{6_{min.}} \cdot v_{6_{max.}}]$$

$$\alpha_{arb} \in [\alpha_{min.} \cdot \alpha_{max.}],$$

$$\beta_{arb} \in [\beta_{min.} \cdot \beta_{max.}]$$

$$Volume_{geometry} \leq Volume_{Max.}$$

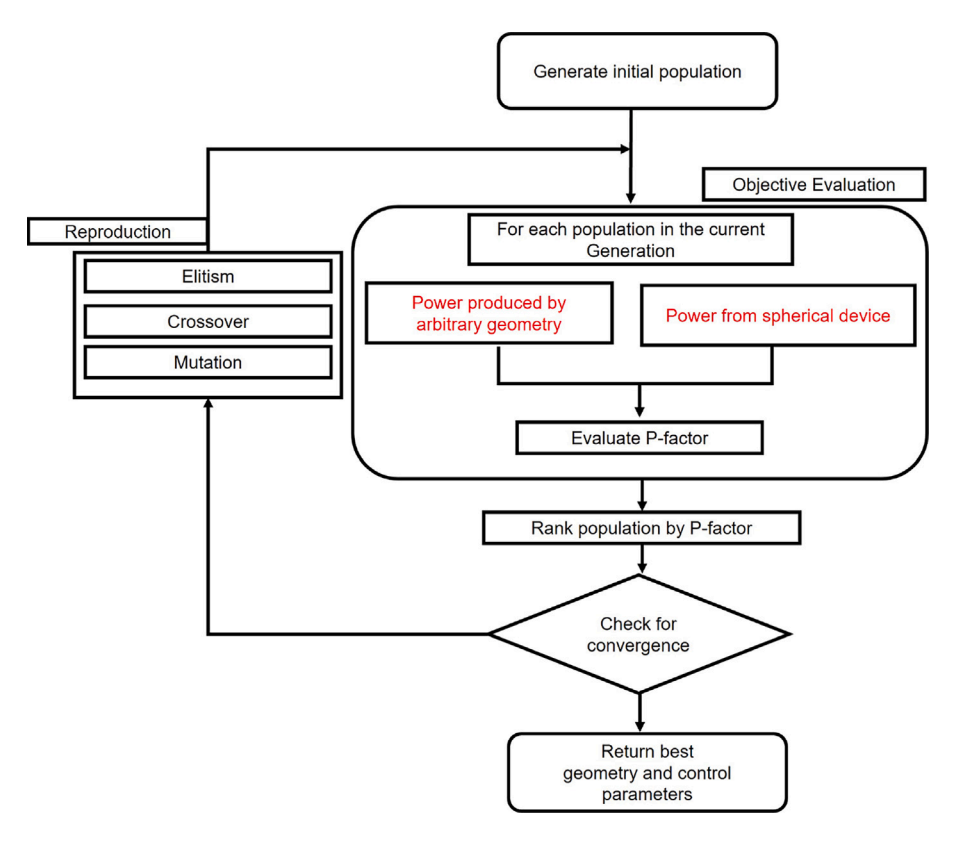


Fig. 9. GA flowchart for control co-design optimization.

Table 2
Lower and upper bounds of design variables.

Parameter	Unit	Lower Bound	Upper Bound
v_1	m	3	15
v_2	m	0	5
v_3	_	0.2	1.5
v_4	_	0.2	1.5
v_5	_	0.2	1.5
v_6	-	0.2	1.5
α_{arb}	-	0.1	3
β_{arb}	-	0.1	3

where v_1 and v_2 are the variables representing the draft and length of the horizontal base, v_3 , v_4 , v_5 , v_6 , are the slopes of the inclined panels, α_{arb} , and β_{arb} are the linear and nonlinear control coefficients for the nonlinear damping control also formulated as:

$$u = -\alpha_{arb}B_{max}(\omega)\dot{z} - \beta_{arb}B_{max}(\omega)\dot{z}^{3}$$
(46)

Finally, the volume of the optimized geometry is constrained not to exceed a set maximum volume, the same as that used in the spherical co-design. Genetic algorithm (GA) is the chosen optimization algorithm. The denominator of the objective is the power from the optimized spherical device in Eq. (45), while the numerator is the power from the arbitrary geometry device. When P>1, this indicates an improved performance by the arbitrary shape over the spherical device; otherwise, p<1 means the arbitrary shape has a worse performance. A flowchart of the geometric optimization of the nonlinear device is presented in Fig. 9; it is important to note that the power from the spherical devices is not recomputed at every optimization step. At the end of the optimization, the optimal shape and control parameters are returned. The optimization variables' bounds are as presented in Table 2.

In setting up the GA for optimization, a number of factors has to be considered. The design space has to be large enough to ensure

Table 3Genetic algorithm optimization variables.

Variable	Value
Population Size	10*N _v
Generations	30
Elite count	5
FunctionTolerance	1e-4

diverse potential solutions. To achieve this, the parameters of GA like the number of population members, generations, the probabilities for crossover and mutation operators has to be selected carefully. The GA parameters used for the optimization in this work are summarized in Table 3. Where N_v is the number of variables in the optimization problem.

5. Numerical simulations

The designated wave site is PacWave South, an approved testing facility set to be built 7 nautical miles (NM) off the central coast of Newport, Oregon. The location provides four test berths located in depths ranging from 65 to 78 m. Its purpose is to address the testing site gap in the United States (US). specifically for wave energy (Batten et al., 2016; Freeman et al., 2022). The annual frequency of occurrence of sea states parameterized in terms of the significant wave heights and energy period is presented in Fig. 10. The prevalent sea state at the PacWave South site typically features a significant wave height of 1.75 m and an energy period of 8.5 s. In contrast, the highest annualized wave energy sea state is characterized by a significant wave height of 2.75 m and an energy period of 10.5 s. (Dunkle et al., 2020). To transform the energy period to peak period, the equation is $T_p = \frac{1}{0.83} T_e$ (Ahn, 2021). The monthly average sea conditions at the site are summarized in Table 4.

Referencing the PacWave generation scenarios presented in Lettenmaier et al. (2022), it can be deduced that two identical point absorber

Table 4
Monthly sea condition at PacWave South.

Average monthly sea condition at PacWave South.			
Month	Significant wave height (m)	Energy period (s)	
January	3.2	11.2	
February	3.1	11.3	
March	2.8	10.8	
April	2.4	10.0	
May	1.9	9.2	
June	1.7	8.8	
July	1.5	8.2	
August	1.5	8.6	
September	1.7	9.2	
October	2.3	10.2	
November	3.0	10.6	
December	3.2	11.2	

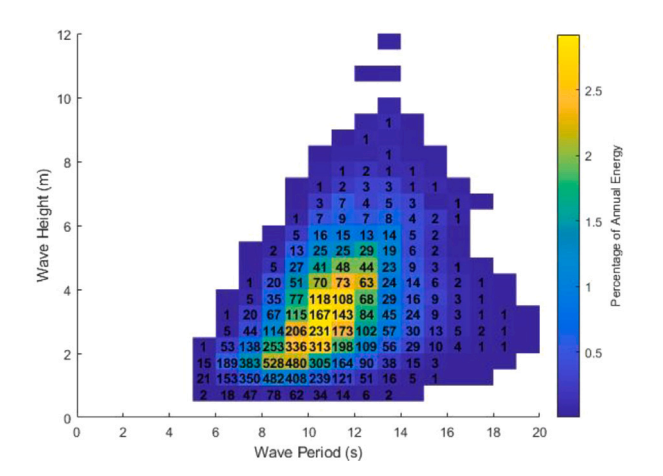


Fig. 10. Sea-state histogram from 1980–2010 at PacWave South (annual mean conditions).

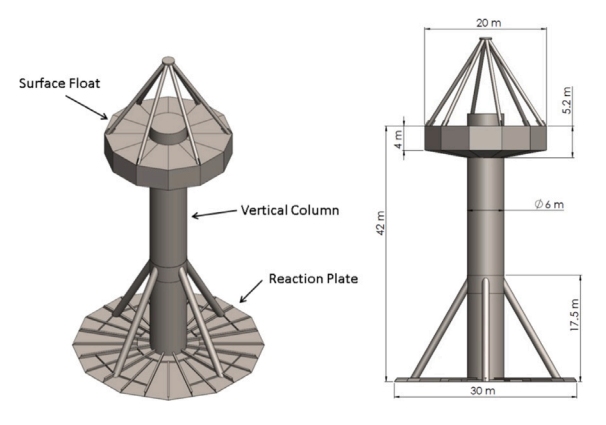


Fig. 11. RM3 device design and dimensions.

wave energy converters (WECs) were deployed at two test berths. Both are a 5-MW peak output power Reference Model 3 (RM3) WEC. The reference model 3 (RM3, USA) is a self-referencing floating point absorber (PA) type WEC Fig. 11. Since the same PacWave site has been chosen for consideration in this work, the maximum reference volume of the nonlinear spherical and arbitrary geometry floater is assumed to be about twice the volume of the RM3 floater, which is calculated to be approximately 1284.4496 m³.

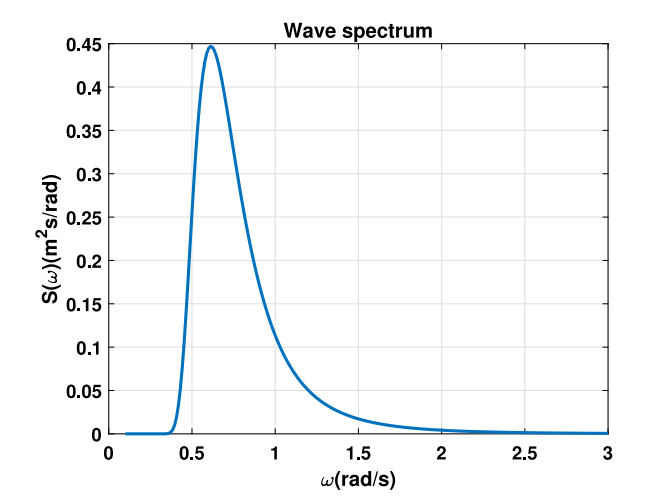


Fig. 12. Wave spectrum.

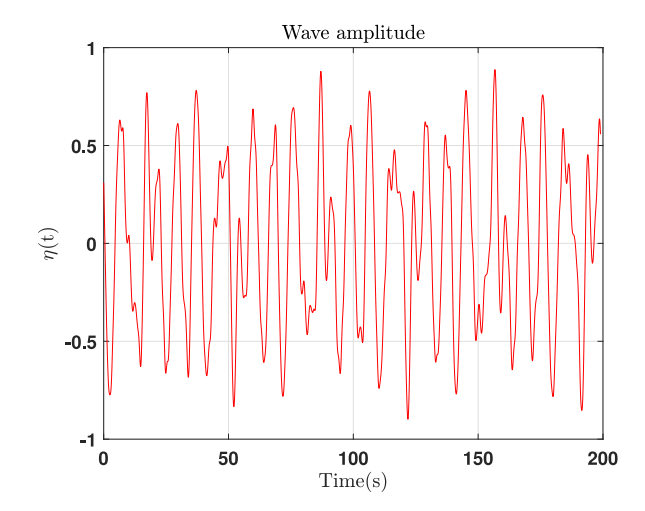


Fig. 13. Wave amplitude.

5.1. Problem setup

The devices are optimized for the most commonly occurring sea state at the PacWave South site, with a significant wave height of 1.75 m and an energy period of 8.5 s considering a Bretschneider spectrum. At the end of the optimization, the performances of both the nonlinear spherical WEC and the arbitrary geometric WEC are computed and compared for the monthly wave condition. The $Volume_{Max}$, which is twice the volume of the RM3 floater, is computed to be approximately 2568.8992 m³. The analytical hydrodynamics solution presented in Section 3 is employed to compute the exact hydrodynamics for equally spaced 34 frequencies between 0.1 and 3.0 rad/s. For the wave spectrum, the time domain wave elevation in the time domain can be computed using multiple sinusoids with different wave amplitudes and random phases using the series:

$$\eta(t) = \sum_{i=1}^{N} a_{i} cos(\omega_{i} t + \phi_{i})$$
 (47)

where a_i is the amplitude, ω_i is the frequency and ϕ_i is the phase. The wave spectrum and amplitude for the significant wave height and frequency are shown in Figs. 12 and 13.

5.1.1. Spherical device co-design optimization

In this section, the resulting optimized spherical devices are presented. The optimal radius and the corresponding control coefficients

Table 5
The optimized parameters for a sphere.

S/N	R	α_s	β_s	Power (W)
1	8.4655	0.2088	0.1113	1.9391e07
2	8.4900	0.1835	0.1119	1.9252e07
3	8.4500	0.2293	0.1081	1.9123e07
4	8.1722	0.2582	0.1112	1.8275e07
5	8.3849	0.3448	0.1047	1.7913e07

Table 6 Optimized parameters.

Parameter	Unit	1	2	3
\mathbf{v}_1	m	8.4041	9.5823	8.3204
\mathbf{v}_2	m	0.2082	0.3546	0.0470
\mathbf{v}_3	_	1.4994	1.4091	1.4669
V_4	-	0.3550	0.2143	0.3420
v ₅	-	0.3929	0.4363	0.6860
v_6	-	0.9738	0.4182	0.6273
α_{arb}	-	0.8967	2.4899	2.6480
β_{arb}	_	0.5222	0.2752	2.1860
Power	W	2.26e08	2.32e08	1.95e08
P	-	1.2116	1.2240	1.0435

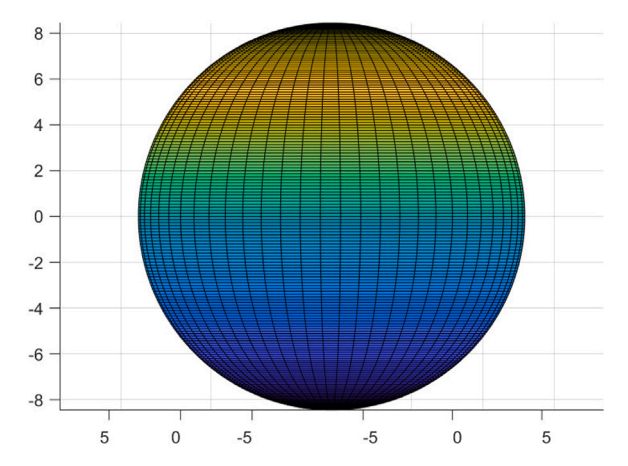


Fig. 14. Optimized nonlinear spherical device.

are tabulated in Table 5. The average power from a 200s time domain optimization run is also tabulated. The optimized device plotted in Fig. 14, with a radius R=8.45 m, and its corresponding power is selected as the base device to be used in the arbitrary geometry optimization.

5.1.2. Co-design of arbitrary shaped WECs

In this section, the optimized spherical device from Section 5.1.1 is the basis for the geometry to be optimized. The optimizer sought to find the combination of optimization variables that achieved better power extraction than the optimized spherical device in the same wave condition and under the same volume constraint. The result of the best-performing geometry is plotted in Fig. 15. The optimizer returned the geometry with minor variations in the variables, some of which are listed in Table 6.

The time domain simulation of optimized geometry is plotted against that of the reference spherical device using constrained and unconstrained control solutions while considering the significant wave condition. Also, the monthly performance of the devices was compared using the average monthly sea condition presented in Table 4.

5.1.3. Performance of an device

In this section, the time domain performance of the optimized shape and the spherical devices. The devices used in this performance simulation are the spherical and the optimized arbitrary geometry 3

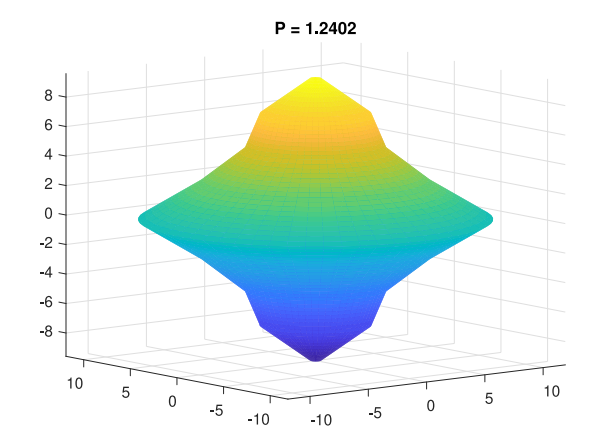


Fig. 15. Performance of optimized geometry using constrained control.

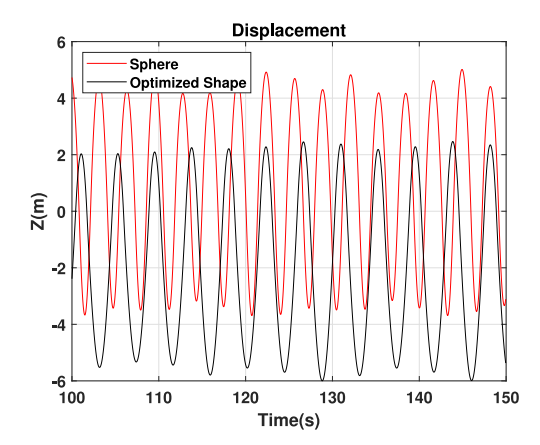


Fig. 16. Velocity of the sphere and optimized geometry using constrained control.

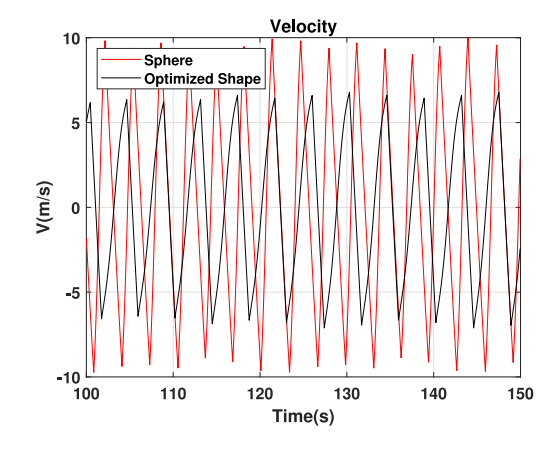


Fig. 17. Velocity of the sphere and optimized geometry using constrained control.

from Table 6. The nonlinear controls co-optimized are applied to the devices while being excited by irregular waves. The resulting performance of both devices is presented. Like the optimization setup, the Bretschneider spectrum was used to generate the irregular waves.

The performance of the optimized geometry in the predominant wave with a significant period of $T_p=10.2409~\rm s$, and significant wave height $H_s=1.75~\rm m$, is plotted in Fig. 15. The optimized geometry was able to achieve a 24% performance improvement over the spherical device.

The displacements, velocities, and PTO forces are plotted in Figs. 16, 17 and 18 respectively. Although an irregular excitation was simulated,

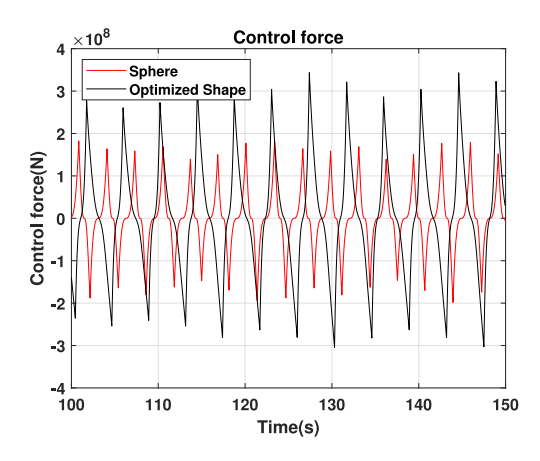


Fig. 18. PTO force of the sphere and optimized geometry using constrained control.

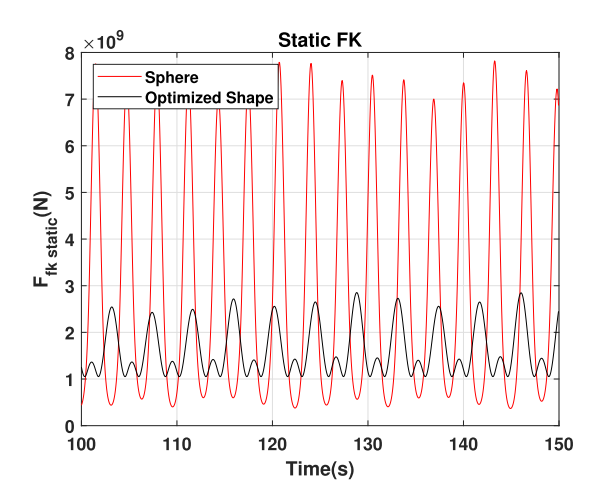


Fig. 19. Static FK force on the devices using constrained control.

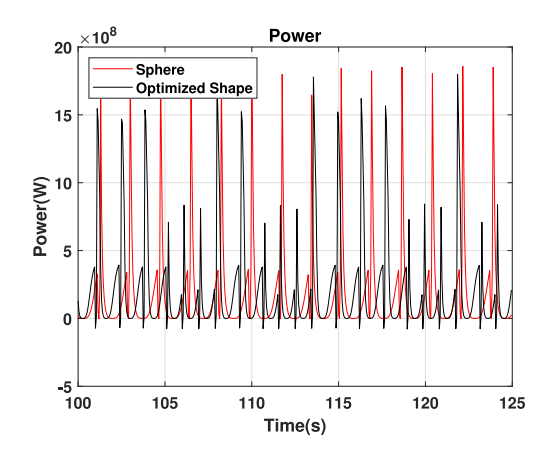


Fig. 20. Power extracted by the sphere and optimized geometry using constrained control.

a regular response was observed; this is due to the controller driving the devices to respond at a particular frequency that maximized the power extraction over the period of operation. The sphere achieves higher velocity, but the optimized geometry's control force is larger than the PTO force exerted on the sphere by the nonlinear control. The nonlinear hydrostatic force on the devices is plotted in Fig. 19; there is a large variation in the forces acting on the spherical device and a relatively small variation in the magnitude of the force on the optimized

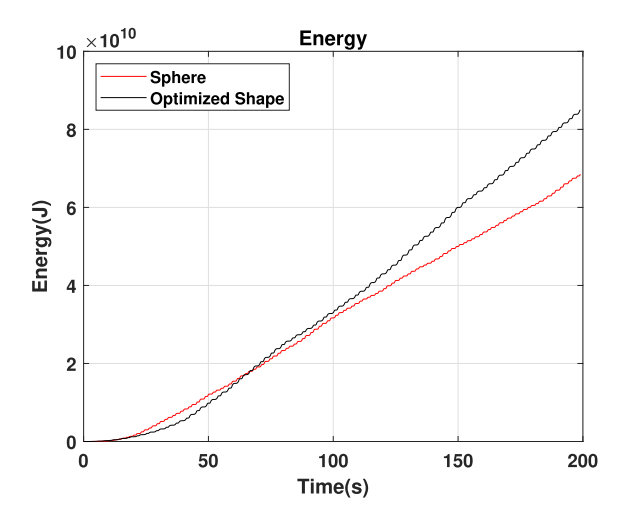


Fig. 21. Energy extracted by the sphere and optimized geometry using constrained control.



Fig. 22. Monthly performance of the sphere and optimized geometry using constrained control.

shape. On average, the hydrostatic force acting on the spherical device geometry is larger than that on the optimized geometry.

The power from the device is calculated as a product of the PTO force and velocity; the power from both devices is as shown in Fig. 20. It can be observed that the power from the optimized geometry has some of the plots below the zero line; this represents the power taken from the grid to drive the system in order to maximize the overall energy extraction, while the spherical devices only extract power from the waves. Fig. 21 is a plot of the cumulative power over the operation time $(E = \int_0^{t_f} \{-u(t)z_2(t)\}dt)$. The plot shows a 24% performance improvement achieved by the optimized shape over the standard spherical buoy. This energy improvement achieved by the optimized geometry is partially due to the reactive power which contributes to the overall energy extraction by the device. The ratio of performances from the devices over the months of the year is plotted in Fig. 22; the performance varies between 10-50%, improvement. Overall, the optimized geometry consistently outperforms the spherical device.

6. Conclusion

In this work, we investigated the control co-design of nonlinear wave energy converters; the geometry of the buoy is modeled as panels which angles are optimized alongside their nonlinear controls, within constraints. The objective is to achieve devices that can leverage the hydrodynamic nonlinear Froude-Krylov forces to improve the power extraction from the waves. An algebraic method of approximating the Froude-Krylov forces was developed to avoid the computationally expensive methods. Time-domain dynamic model coupled with a nonlinear control formulation was used to compute the power to ensure the most realistic results. An analytic method of computing the hydrodynamic coefficients (added mass and radiation damping) based on variable separation and eigenfunction expansion was developed for use in the optimization; this analytic approach for hydrodynamics calculations is critical for efficient numerical optimization. The performance of the optimized device in the various wave conditions of the PacWave site is presented. The performance of the optimized device yielded an average of 20% improvement over the spherical device. Overall, in all simulations, the optimized geometry was found to have leveraged the hydrodynamic nonlinearity better than the spherical device. The optimized device consistently outperformed the spherical device in all wave conditions of the different months of the year. Future work will investigate how an array of nonlinear devices can leverage these nonlinearities and the inter-device hydrodynamic coupling.

CRediT authorship contribution statement

Habeebullah Abdulkadir: Writing – review & editing, Writing – original draft, Methodology, Investigation, Conceptualization. **Ossama Abdelkhalik:** Investigation, Funding acquisition, Conceptualization, Software, Supervision, Writing – review & editing.

Declaration of competing interest

The authors declare that they have no known competing financial interests or personal relationships that could have appeared to influence the work reported in this paper.

Data availability

No data was used for the research described in the article.

References

- Abdelkhalik, O., Darani, S., 2018. Optimization of nonlinear wave energy converters. Ocean Eng. 162, 187–195.
- Ahn, S., 2021. Modeling mean relation between peak period and energy period of ocean surface wave systems. Ocean Eng. 228, 108937.
- ANSYS, A., 2013. Version 15.0. vol. 752, ANSYS Inc., Canonsburg, PA, USA, November. Babarit, A., Delhommeau, G., 2015. Theoretical and numerical aspects of the open source BEM solver NEMOH. In: 11th European Wave and Tidal Energy Conference. (EWTEC2015).
- Bacelli, G., Genest, R., Ringwood, J.V., 2015. Nonlinear control of flap-type wave energy converter with a non-ideal power take-off system. Annu. Rev. Control 40, 116–126.
- Batten, B., Polagye, B., LiVecchi, A., 2016. Northwest National Marine Renewable Energy Center. Technical Report, Oregon State Univ., Corvallis, OR (United States). Chamberlain, P., Porter, D., 1999. On the solution of the dispersion relation for water waves. Appl. Ocean Res. 21 (4), 161–166.
- Child, B., Venugopal, V., 2010. Optimal configurations of wave energy device arrays. Ocean Eng. 37 (16), 1402–1417.
- Coe, R.G., Bacelli, G., Olson, S., Neary, V.S., Topper, M.B., 2020. Initial conceptual demonstration of control co-design for WEC optimization. J. Ocean Eng. Mar. Energy 6 (4), 441–449.
- Davidson, J., Windt, C., Giorgi, G., Genest, R., Ringwood, J.V., 2019. Evaluation of energy maximising control systems for wave energy converters using openfoam. In: OpenFOAM®: Selected Papers of the 11th Workshop. Springer, pp. 157–171.
- Demonte Gonzalez, T., Parker, G.G., Anderlini, E., Weaver, W.W., 2021. Sliding mode control of a nonlinear wave energy converter model. J. Mar. Sci. Eng. 9 (9), 951.

- Dunkle, G., Robertson, B., García-Medina, G., Yang, Z., 2020. Pacwave wave resource
- Freeman, M.C., O'Neil, R., Garavelli, L., Hellin, D., Klure, J., 2022. Case study on the novel permitting and authorization of PacWave south, a US grid-connected wave energy test facility: Development, challenges, and insights. Energy Policy 168, 113141.
- Garcia-Sanz, M., 2019. Control co-design: an engineering game changer. Adv. Control Appl.: Eng. Ind. Syst. 1 (1), e18.
- Garcia-Teruel, A., Forehand, D., 2021. A review of geometry optimisation of wave energy converters. Renew. Sustain. Energy Rev. 139, 110593.
- Giannini, G., Rosa-Santos, P., Ramos, V., Taveira-Pinto, F., 2022. Wave energy converters design combining hydrodynamic performance and structural assessment. Energy 249, 123641.
- Giorgi, G., Ringwood, J.V., 2017. Computationally efficient nonlinear Froude–Krylov force calculations for heaving axisymmetric wave energy point absorbers. J. Ocean Eng. Mar. Energy 3, 21–33.
- Giorgi, G., Ringwood, J.V., 2018. A compact 6-dof nonlinear wave energy device model for power assessment and control investigations. IEEE Trans. Sustain. Energy 10 (1), 119–126.
- Giorgi, G., Sirigu, S., Bonfanti, M., Bracco, G., Mattiazzo, G., 2021. Fast nonlinear Froude-Krylov force calculation for prismatic floating platforms: A wave energy conversion application case. J. Ocean Eng. Mar. Energy 7 (4), 439–457.
- Guo, B., Ringwood, J.V., 2021a. Geometric optimisation of wave energy conversion devices: A survey. Appl. Energy 297, 117100.
- Guo, B., Ringwood, J.V., 2021b. A review of wave energy technology from a research and commercial perspective. IET Renew. Power Gener. 15 (14), 3065–3090.
- Jefferys, E., 1984. Simulation of wave power devices. Appl. Ocean Res. 6 (1), 31-39.
- Jin, S., Patton, R.J., Guo, B., 2019. Enhancement of wave energy absorption efficiency via geometry and power take-off damping tuning. Energy 169, 819–832.
- Kokkinowrachos, K., Mavrakos, S., Asorakos, S., 1986. Behaviour of vertical bodies of revolution in waves. Ocean Eng. 13 (6), 505–538.
- Korde, U.A., Ringwood, J., 2016. Hydrodynamic Control of Wave Energy Devices. Cambridge University Press.
- Lettenmaier, T., Gevorgian, V., Antonishen, M., 2022. PacWave Grid Integration Study: Transient and Dynamic Conditions-Final Report. Technical Report, National Renewable Energy Lab.(NREL), Golden, CO (United States).
- McNatt, J.C., Venugopal, V., Forehand, D., 2015. A novel method for deriving the diffraction transfer matrix and its application to multi-body interactions in water waves. Ocean Eng. 94, 173–185.
- Na, J., Wang, B., Li, G., Zhan, S., He, W., 2018. Nonlinear constrained optimal control of wave energy converters with adaptive dynamic programming. IEEE Trans. Ind. Electron. 66 (10), 7904–7915.
- Ochs, M.E., Bull, D.L., 2013. Technological Cost-Reduction Pathways for Oscillating Water Column Wave Energy Converters in the Marine Hydrokinetic Environment. Technical Report, Sandia National Lab.(SNL-NM), Albuquerque, NM (United States).
- O'Sullivan, A.C., Lightbody, G., 2017. Co-design of a wave energy converter using constrained predictive control. Renew. Energy 102, 142–156.
- Pao, L.Y., Zalkind, D.S., Griffith, D.T., Chetan, M., Selig, M.S., Ananda, G.K., Bay, C.J., Stehly, T., Loth, E., 2021. Control co-design of 13 MW downwind two-bladed rotors to achieve 25% reduction in levelized cost of wind energy. Annu. Rev. Control 51, 331–343
- Richter, M., Magana, M.E., Sawodny, O., Brekken, T.K., 2012. Nonlinear model predictive control of a point absorber wave energy converter. IEEE Trans. Sustain. Energy 4 (1), 118–126.
- Song, J., Abdelkhalik, O., Zou, S., 2020. Genetic optimization of shape and control of non-linear wave energy converters. In: International Conference on Offshore Mechanics and Arctic Engineering, vol. 84416, American Society of Mechanical Engineers, V009T09A036.
- WAMIT User Manual, V., 2013. 7.0. WAMIT Inc., Chestnut, MA, USA.
- Wilson, D.G., Bacelli, G., Robinett, III, R., Abdelkhalik, O., 2018. Nonlinear Control Design for Nonlinear Wave Energy Converters. Technical Report, Sandia National Lab.(SNL-NM), Albuquerque, NM (United States).
- Wilson, D.G., Robinett, III, R.D., Bacelli, G., Abdelkhalik, O., Coe, R.G., 2020. Extending complex conjugate control to nonlinear wave energy converters. J. Mar. Sci. Eng. 8 (2) 84
- Yilmaz, O., 1998. Hydrodynamic interactions of waves with group of truncated vertical cylinders. J. Waterw. Port Coast. Ocean Eng. 124 (5), 272–280.
- Zhang, W.C., Liu, H.X., Zhang, L., Zhang, X.W., 2016. Hydrodynamic analysis and shape optimization for vertical axisymmetric wave energy converters. China Ocean Eng. 30, 954–966.
- Zou, S., Song, J., Abdelkhalik, O., 2023. A sliding mode control for wave energy converters in presence of unknown noise and nonlinearities. Renew. Energy 202, 432–441.